Growth of Nanocolumnar Porous TiO_2 Thin Films by Magnetron Sputtering using Particle Collimators

A. Garcia-Valenzuela[1], R. Alvarez[1,2*], V. Rico[1], J. Cotrino[1,3], A.R. Gonzalez-Elipe[1], A. Palmero[1*]

[1] Instituto de Ciencia de Materiales de Sevilla (CSIC-US), Américo Vespucio 49, 41092 Seville, Spain

[2] Departamento de Física Aplicada I. Escuela Politécnica Superior. Universidad de Sevilla. c/ Virgen de África 7, 41011, Seville, Spain

[3] Departamento de Física Atómica, Molecular y Nuclear. Universidad de Sevilla. Avda. Reina Mercedes s/n, 41012 Seville, Spain

Abstract

The selective incorporation of deposition species with preferential directionality is analyzed during the growth of TiO_2 thin films by magnetron sputtering. Using wisely-designed collimators, tilted nanocolumnar morphologies are grown in a ballistic deposition regime, i.e. when most deposition species arrive at the film surface along well-defined preferential directions, and also in a thermalized deposition regime, when these species follow an isotropic momentum distribution in the plasma gas. The obtained results suggest that the use of particle collimators may promote the growth of porous thin films even in the classical magnetron sputtering configuration, when the target and the substrate are parallel. General insights are given on this approach and, as a proof of concept, its principles applied for the synthesis of nanostructured films in a laboratory-size reactor.

Keywords: Reactive Magnetron Sputtering, TiO_2, Oblique Angle Deposition, Porous Thin Films, PVD, GLAD.

*Email: rafael.alvarez@icmse.csic.es; alberto.palmero@csic.es

Introduction

The magnetron sputtering (MS) technique is a robust deposition method widely employed in the industry and in research centers [1]. It makes use of a low pressure plasma, usually argon, to interact with a solid target from which atoms are sputtered and subsequently deposited onto a substrate [2]. Even though this technique has been traditionally aimed at growing compact and dense thin films [3, 4, 5], new geometrical configurations are being nowadays implemented to widen its possibilities and tailor the film microstructure [6, 7]. This is the case of the so-called oblique angle deposition (OAD) configuration, well-known for promoting the growth of porous layers of great utility in numerous technological fields, e.g. optical and electrical devices [8, 9, 10], sensors [11, 12], electrodes for solar cells [13] or biomedicine [14], among others [6]. In this regard, the OAD configuration promotes the oblique arrival of deposition species onto a substrate (usually achieved by tilting it with respect to the target [15, 16]) to induce surface shadowing processes leading to the formation of well-separated and tilted columnar porous structures with diameters in the order of few tens nanometer [17], very similar to those obtained by evaporation at oblique angles [18, 19].

The formation and development of nanocolumnar porous structures in MS-OAD is intimately related to the control of the momentum distribution of sputtered species in the plasma gas and, in particular, to their incidence onto the substrate along certain preferential directions [6]. In general, particles are sputtered from the racetrack, which is the region of the target with maximum ion impingement from the plasma, as visualized by a ring of light [20]. When sputtered, particles follow a typical cosine-type angular distribution and, according to the Thomson formula, an energy distribution that peaks around ~U/2, where U is the binding energy of target surface atoms [1]. Yet, the presence of a plasma gas in the reactor introduces the possibility of different scattering processes in their way from the target to the film that may modify both distributions [21, 22]. In this context, the so-called ballistic species correspond to those that do not undergo any collision with gas species, thus keeping their original momentum and energy when deposited. On the other hand, sputtered species that experience a large number of collisions in the plasma

gas and, hence, possess an isotropic momentum distribution [23], are called thermalized species, with typical kinetic energies below 0.1 eV. Finally, a third component corresponds to those sputtered species that are partially thermalized, i.e. those that have undergone several collisions in the gas phase, but their momentum distribution still shows a certain preferential direction. In this way, and from a qualitative point of view, the non-dimensional parameter, Ξ, dubbed thermalization degree, describes the balance between these components. It is defined as $\Xi = L/\lambda\nu$, with L the distance between the target and the film, λ the mean free path of sputtered species in the plasma gas and ν the average number of elastic scatterings a sputtered species requires to become thermalized with the gas, as obtained by Westwood in ref. [24]. In general, Ξ depends on numerous quantities, such as the masses and atomic radii of sputtered and plasma heavy species, the target-substrate distance or the gas pressure and temperature, among others [25]. In this way, the condition $\Xi \ll 1$ implies a low amount of collisions, meaning that most sputtered species remain ballistic [26], while the condition $\Xi \gtrsim 1$ implies that collisions are so numerous that all sputtered species can be considered thermalized with the plasma gas [27]. However, and due to the stochastic character of the collisional transport of sputtered species, when Ξ is in the mid-range, the three types of species (ballistic, thermalized and partially-thermalized) coexist and contribute to the film growth [28].

Ballistic species arrive along well-defined preferential directions at the substrate and are responsible for the formation of tilted nanocolumnar arrays when operating at oblique angles [6]. Thermalized species, on the other hand, tend to form vertically-aligned coalescent nanostructures, whose diameter increases with the film height [29]. In fact, the actual film nanostructure emerges from the competition between these two trends, in such a way that highly porous nanocolumanr thin films can solely be obtained when the ballistic component dominates over the rest (for instance, targeting the $\Xi \ll 1$ condition by decreasing the plasma gas pressure) [27]. Yet, the minimum operational deposition pressure during film growth is usually limited by the necessity to maintain a plasma discharge in the reactor, thus constraining the value of Ξ above a certain threshold. In this paper, we analyze how deposition species with either isotropic or specific

directionalities in the plasma gas can be selected by using particle collimators under a variety of magnetron sputtering operating conditions, studying their influence on the film nanostructure. Moreover, based on the results presented in this paper, we perform a proof of concept of a reactor that, operating under the classical magnetron sputtering arrangement, has been used to grow porous thin films with the help of a collimator. For this investigation we have employed TiO_2 as test material due to its relevance in numerous applications [30, 31], although our results can be easily extrapolated to other materials or situations.

Experimental Setup

A set of amorphous TiO_2 thin films were grown using the reactive magnetron sputtering technique [3] in the deposition setup described in ref. [29]. A 3 inches diameter titanium target was employed, placing the substrate holder at a distance, L=7 *cm*. A collimator made of aluminum with a base length of L_C=*2 cm* was designed with a 20º angular aperture, aiming at covering 1 cm x 1 cm samples, as shown in figure 1a. Deposition time in each case was chosen to grow films with thicknesses between 200 and 500 nm, as determined by means of cross-sectional Field Emission Scanning Electron Microscopy (FESEM) images. The base pressure of the deposition reactor was 7×10^{-4} Pa. The oxygen partial pressure during depositions was kept at 0.05 Pa, which was enough to operate in the oxidic mode of the discharge [32, 33] and get fully oxidized films. This operational mode is known for promoting low growth rates, which is why deposition times as long as few hours were required (see Table I for specific values).

Samples were prepared using the deposition conditions listed in Table I. In conditions #1-#6, substrates were tilted with respect to the target surface to achieve an 80º alignment between the racetrack and the substrate or, likewise, an 80º incidence with respect to the substrate normal of species sputtered over the growing film. Since the racetrack had a radius of ~2 cm, there is a shift of ~15º between the substrate tilt angle and the incident polar angle aligning the racetrack and the film surface. Hence, to achieve a polar angle of incidence of 80º, a substrate rotation of 95º was

imposed, as depicted in figure 1b, in a configuration that also affects the incident azimuthal angle distribution (for more details on the relation between the tilt angle of the substrate and the angle of incidence of the sputtered species see ref. [34]). A second collimator was employed in case #7, with base length L_C=5 *cm* and L=10 *cm*. Further details are given in the Results and Discussion section.

The incident polar angle distribution of deposition species as a function of the experimental conditions (reactor geometry, tilt angle of the substrate and other geometrical constrains such as particle collimators) was calculated by the well-known and widely accepted SIMTRA code [35, 36]. This software describes the collisional transport of sputtered species through the plasma gas by means of binary collisions for a given chemical nature of the species, reactor geometry, background gas pressure and temperature, racetrack features, etc. The angle and energy distribution of sputtered species at the target are calculated by the software SRIM [37], a well-accepted software to describe the ion-assisted sputtering process [1]. An average gas temperature of 350 K and a screened Coulomb potential (Molière type) were considered in the simulations along with a circular racetrack with radius 2 cm. Finally, UV-vis absorption spectroscopy was employed to determine the refractive index of the deposited films which, for the purpose of the present work, will be taken as an indirect way of assessing their porosity. Transmittance spectra of TiO_2 thin films deposited on quartz were analyzed by the home-made MATLAB-based software, OPTIFIT [38], to estimate the refractive indexes of the layers. The obtained optical functions have been corroborated by simulating the reflectance spectrum of each layer and comparing them with the corresponding experimental profiles, finding a good agreement in all studied cases (see supporting information for more details).

Results and Discussion

In figure 2a we present the incident polar angle distribution corresponding to conditions #1 in Table I, as calculated by the SIMTRA code (for simplicity we analyze the polar angular

distribution, as obtained by integrating the total angular distribution with respect to the azimuthal angle). The curve shows a well-defined peak for an incidence of 80º with respect to the target normal and a relevant contribution of species that arrive at less oblique angles. The amount of ballistic, thermalized and partially-thermalized species that contribute to the growth can be assessed by splitting this incident polar angle distribution into three components, according to the kinetic energy of each species. In this way, we consider that thermalized species arrive at the film surface with kinetic energies below 0.1 eV, ballistic species with energies above $U/2$, and partially-thermalized species with energies in the range between 0.1 and $U/2$ (in this paper, and in agreement with the software SRIM, U has been estimated ~5 eV). The relation between a given collisional transport (i.e., number of collisions in the plasma gas) and the kinetic energy of deposition species is not straightforward and strongly depends on the energy distribution of sputtered species and the particular interaction potential under consideration. Therefore, the energy threshold U/2 must be understood as a qualitative limit to differentiate the species whose momentum distribution has not been significantly altered and arrive along a well-defined direction at the substrate. These three components have been included in figure 2a, where it is evident a clear peak centered at 80º, corresponding to the ballistic contribution and a broad distribution of thermalized species centered at about 45º. There is also a third contribution of partially-thermalized species, with a maximum at about 65º. For these working conditions, the following proportions between species are obtained: 21% ballistics, 21% partially thermalized and 58% thermalized. This partition agrees with the qualitative estimation of $\Xi \sim 13.2 p_g L$ $(Pa^{-1}\, m^{-1})$ in our conditions [25], with p_g the deposition pressure. The operating values of p_g and L in our case yield $\Xi \sim 0.5$, i.e., a mid-range condition where deposition species are expected to be half-way between purely ballistic and fully thermalized.

The cross-sectional SEM image of sample #1 appears in figure 3a and is characterized by almost vertical coalescent structures, whose diameter increases with height. According to refs. [29, 39], this nanostructure emerges when a high proportion of thermalized species contributes to the growth of the film (a minor amount of ballistic species is evidenced by the small ~10º tilt of these

structures). The refractive index of sample #1 is $n_{\#1} = 2.0$, which contrasts with the value $n = 2.4$ obtained for a full compact layer of this material. This suggests the existence of some porosity in sample #1: according to the Bruggeman effective medium approximation, porous layers can be taken as a physical mixture of the air filling the voids and TiO_2, rendering a lower value of the measured refractive index [40]. As mentioned above, the ballistic contribution in figure 2a peaks at 80º and covers an angular width of ~20º, while the angular distributions of thermalized and partially thermalized species are much wider and peak at 45º and ~65º, respectively. This means that the influence of these two latter species can be minimized by placing a 20º aperture collimator pointing to the racetrack of the target (c.f., Figure 1a-b). The calculated incident polar angle distribution for conditions #2, i.e., same conditions as #1 but using the collimator at the substrate location, appear in figure 2a, where it is clear that this specific configuration allows the selection of incident polar angles between 70º and 90º. The SEM image of sample #2 in figure 3b shows a ~50º tilted and well-defined columnar microstructure, which must be associated to the dominant contribution of ballistic species with well-defined preferential directionality. The calculated refractive index in this case is $n_{\#2} = 1.8$, a lower value than that of sample #1, a result that sustains a higher porosity for this layer.

Based on the results above, cases #3 and #4 are next analyzed: sample #3 was grown without collimator at a pressure of 0.2 Pa, or likewise for $\Xi \sim 0.2$, i.e. under conditions where the ballistic contribution is expected to dominate over the other two. The calculated incident polar angle distribution function appears in figure 2b, showing the existence of a dominant ballistic contribution (55%), and minor contributions of thermalized and partially thermalized species (17% and 28%, respectively). The cross-sectional SEM image of sample #3, depicted in figure 3c, shows a ~25º tilted columnar nanostructure very similar to that reported in the literature for these conditions and oblique angles [6]. The refractive index amounts $n_{\#3} = 1.9$, showing that sample #3 possesses a porous morphology. Yet, when growing the film under conditions #4, i.e., same conditions as in #3 but using the particle collimator, the incident polar angle distribution function in figure 2b narrows down to angles between ~70º and 90º, minimizing the incorporation

of thermalized and partially-thermalized species. The cross-sectional SEM image of sample #4 in figure 3d depicts a film formed by ~50º tilted nanocolumnar structures with a refractive index $n_{\#4} = 1.8$ (i.e. it shows a better defined nanostructure than case #3 in figure 3c), where columns are more tilted and the film more porous. Remarkably, samples #2 and #4 in figures 3b and 3d possess very similar nanostructures and refractive indexes. This result must be an effect of the particle collimator, which successfully provokes the selective deposition of highly directed species. In fact, and even though samples #2 and #4 were prepared at different pressures, the collimation of highly directed species in either case causes that the incident polar angle distribution functions become rather similar for the two samples (c.f., figure 2a and 2b).

Samples #5 and #6 were deposited at a pressure of 0.8 Pa, or likewise for a value of $\Xi \sim 0.8$, which should qualitatively render a rather negligible amount of ballistic species even in the absence of a collimator. The calculated incident polar angle distribution for conditions #5 represented in figure 2c clearly shows minor ballistic and partially-thermalized components, and a major proportion of thermalized species (77%). For illustration purposes, we have also included in figures 2a-c the theoretical shape of the incident polar angle distribution of species with an isotropic momentum distribution in the gas phase (i.e. thermalized species), $f_{th}(\theta)\, d\theta \propto sin\theta\, cos\theta\, d\theta$ [39], finding a remarkable good agreement with our SIMTRA calculations. The cross-sectional SEM image of the film grown under conditions #5 (see figure 3e) depicts a nanostructure very similar to that of sample #1, characterized by vertical and coalescent nanostructures whose diameter increases with the film height, a feature that we attribute to the large amount of thermalized species in the deposition. However, the refractive index of sample #5 was lower than that of sample #1, with a value of $n_{\#5} = 1.9$ indicating a higher porosity. Remarkably, when using the particle collimator under the same conditions, i.e. conditions #6, a relatively narrow incident polar angle distribution of thermalized species is selected for angles comprised between ~60º and ~90º (see figure 2c). According to the SEM image in figure 3f, it seems that the particle collimator has profoundly affected the microstructure of the film, which now possesses a tilted nanocolumnar morphology, very alike to those presented in cases #2 and

#4 (figures 3b and 3d). In fact, the similar value of the refractive index in this case, $n_{\#6} = 1.8$, suggests a similar porosity in all these three cases.

The results obtained above suggest that, as long as the particle collimator is mounted onto the substrate, similar porous nanostructures can be grown no matter whether the deposition regime is ballistic or thermalized. While ballistic depositions under OAD conditions have been broadly analyzed in the literature by tilting the substrate with respect to the film [6], to our knowledge, the growth of thin films at oblique angles under a thermalized regime has not yet been explored. In fact, this latter possibility would facilitate operating under classical MS configurations (where target and substrate are parallel), as the isotropic momentum of sputtered species in the gas phase would make the results rather independent of the tilt angle of the substrate. In practice, this arrangement could be used to grow porous thin films in reactors where tilting the substrate with respect to the target is not possible due to experimental constrains (e.g. for large substrates), or whenever the operational pressure range forbids a pure ballistic deposition regime. To prove this idea, we have used the same laboratory–size reactor utilized for the preparation of the 1cm^2 samples #1-#6, to make a proof of concept and coat a relatively larger 3 cm long substrate under high thermalization conditions, $\Xi \sim 1.1$ (conditions #7 in Table I). For this preparation, the substrate was placed within a larger collimator (described in the Experimental Setup section), 1 cm apart from its open side and placed parallel to the target, as depicted in figure 1c. The evolution of film thickness and nanostructure along the length of this sample (dotted line in figure 1c, with origin at the collimator vertex) are shown in figure 4a, where we notice a film thickness of around 800 nm near the collimator entrance that falls to values around 100 nm at the other side. Film thickness variations are common in MS-OAD when tilting the substrate in ballistic deposition regimes, since one side of the film is always closer to the target (in the absence of particle collimators we estimate that it is about ~20% along 1 cm long sample). Yet, particle collimators seem to enhance this effect, as the restriction they impose on the incident polar angles is different at either side of the film (see figure 4b). Moreover, it is noteworthy the similar microstructure of the film along its length and the different value of the tilt angle of the nanocolumns (~ 25º) when

compared with sample #6 (c.f. figure 3f), prepared using a smaller collimator that was oriented towards the racetrack and under a nearly-thermalized deposition regime. This is explained in figure 4c, where we show the incident polar angle distribution of deposition species at different positions inside the collimator: although the distributions are rather broad, some variations are appreciable finding that the mean angle of incidence varies from ~55º near the open side of the collimator, to ~70º near the vertex, which are clearly lower than the ~80º incidence in cases #2, #4 and #6 (cf. figures 3b, 3d, 3f). However, and despite the high thickness inhomogeneity of film #7, refractive index in this case was roughly estimated as ~1.8, i.e. similar to that in case #6.

Based on the results above, it seems that while the film nanostructure stays rather homogeneous over the film surface, its thickness is very inhomogeneous, a feature that may represent a serious drawback for practical purposes. In this regard, the previous proof of concept constitutes a first step aimed at understanding the basic principles of particle transport and deposition in the presence of a collimator. For practical applications, with large reactors and larger substrate areas, there are still numerous experimental issues that should be sorted out to implement this process. For example, a collimated roll-to-roll system would contribute to average the thickness of the porous film over the whole substrate. Other adjustments or the use of other movable elements should be also taken into account for a straightforward engineering solution towards the synthesis of porous thin films using MS on large surfaces.

Conclusions

In this paper we have analyzed the influence of using particle collimators to selectively deposit sputtered species with preferential directionality. The proposed approach improves the classical method that relies on minimizing the plasma pressure, and consequently the thermalization degree of the sputtered species. We have also shown that particle collimators allow the growth of highly porous nanocolumnar thin films no matter the thermalization degree of sputtered particles. Evidences of this possibility have been obtained for a series of TiO_2 thin films prepared with this

methodology and characterized by lower refraction indices that their compact counterpart. It is also found that by using collimators, similar well-defined tilted nanocolumnar structures can be prepared no matter the plasma pressure during deposition. This feature, associated to the collimation of the deposition flux, opens up numerous possibilities for thin film nanostructuration when using reactors and/or targets whose operational plasma pressure range or geometrical constrains do not allow pure ballistic deposition regimes or substrate tilt. In this line, we have performed a proof of concept in our laboratory-size reactor under a configuration based on the classical magnetron sputtering geometry to deposit porous nanocolumnar thin films, which sustains the feasibility of this approach for a future up-scaling of the technology.

Acknowledgements

Authors acknowledge the University of Seville (VPPI-US), the Junta de Andalucía (TEP8067, TEP5283 and P12–2265MO) and the Ministry of Economy and Competitiveness of Spain (MAT2013-42900-P, MAT2013-40852-R, MAT2016-79866-R, MAT2015-69035-REDC) for financial support.

References

[1] Reactive Sputter Deposition, Springer Series in Materials Science, D. Depla, S Mahieu, Eds. ISBN 978-3-540-76662-9 Springer-Verlag Berlin, Heildelberg 2008.

[2] D. Cristea, D. Constantin, A. Crisan, C.S. Abreu, J.R. Gomes, N.P. Garradas, E. Alves, C. Moura, F. Vaz, L. Cunha, Vacuum 98, 63 (2013)

[3] J. Borges, N. Martin, N.P. Barradas, E. Alves, D. Eyidi, M.F. Beaufort, J.P. Riviere, F. Vaz, L. Marques, Thin Solid Films 520(21), 6709 (2012)

[4] X. Noirfalise, T. Godfroid, G. Guisbiers, R. Snyders, Acta Materialia 59(20), 7521 (2011)

[5] I. Safi, Surf. Coat. Technol 127, 203 (2000).

[6] A. Barranco, A. Borras, A.R. Gonzalez-Elipe, A. Palmero, Prog. Mater. Sci. 76, 59 (2016)

[7] J. Lintymer, J. Gavoille, N. Martin, J. Takadoum, Surf. Coat. Technol. 174, 315 (2003)

[8] .W. Leem, J.S. Yu, Optics Express 19(10), 258 (2011)

[9] R. El Beainou, N. Martin, V. Potin, P. Pedrosa, MAP Yazdi, A. Billard, Surf. Coat. Technol. 313, 1 (2017)

[10] P. Pedrosa, A. Ferreira, J-M. Cote, N. Martin, M. Arab, P. Yazdi, S. Lanceros-Mendez, F. Vaz, Appl. Surf. Sci. **420**, 681 (2017).

[11] K. Lee, Y.S. Shim, Y.G. Song, S.D. Han, Y.S. Lee, C.Y. Kang, Sensors **17**(2), 303 (2017)

[12] J. Ollitrault, N. Martin, J.Y. Rauch, J.B. Sanchez, F. Berger, Mat. Lett. **155**, 1 (2015)

[13] Y. Liu, Y. Zhao, Y. Feng, J.S. Shen, X.Y. Liang, J. Huang, J.H. Min, L.J. Wang, W.M. Shi, Appl. Surf. Sci 363, 252 (2016)

[14] I. Izquierdo-Barba, J.M. Garcia-Martin, R. Alvarez, A. Palmero, J. Esteban, C. Perez-Jorge, D. Arcos, M. Vallet-Regí, Acta Biomaterialia 15, 20 (2015)

[15] D. Toledano, R. E. Galindo, M. Yuste, J.M. Albella, O. Sanchez, J. Phys. D: Appl. Phys 46, 045306 (2013)

[16] T. Nyberg, C. Nender, H. Högberg, S. Berg, Surf. Coat. Technol. 94, 242 (1997)

[17] V. Collado, N. Martin, P. Pedrosa, Y.-Y. Rauch, M. Horakova, M. A. P. Yazdi, A. Billard, Surf. Coat Technol. 304, 476 (2016)

[18] J.D. Krabbe, V. Keontyev, M.T. Teschuk, A. Kovalenko, M.J. Brett, J. Appl. Phys. 111(6), 064314 (2012)

[19] R. Alvarez, C. Lopez-Santos, J. Parra-Barranco, V. Rico, A. Barranco, J. Cotrino, A. R. Gonzalez-Elipe, A. Palmero, J. Vac. Sci. Technol. B 32(4), 041802 (2014)

[20] Y. Ohtsu, T.Tsuruta, T. Tabaru, M. Akiyama, Surf. Coat. Technol. 307, 1134 (2016)

[21] J. Vac. Sci. Technol. 15, 1 (1978)

[22] A. Palmero, H. Rudolph, F.H.P.M. Habraken, Thin Solid Films 515(2), 631 (2006)

[23] R. Snyders, J.-P. Dauchot, M. Hecq, Plasma Proces. Polym. 4, 113 (2007)

[24] W. D. Westwood, J. Vac. Sci. Technol. 15, 1 (1978)

[25] R. Alvarez, J.M. Garcia-Martin, M.C. Lopez-Santos, V. Rico, F.J. Ferrer, J. Cotrino, A. R. Gonzalez-Elipe, A. Palmero, Plas. Process. Poly. 11, 571 (2014)

[26] R. Alvarez, J. M. Garcia-Martin, A. Garcia-Valenzuela, M. Macias-Montero, F. J. Ferrer, J. Santiso, V. Rico, J. Cotrino, A. R. Gonzalez-Elipe and A. Palmero, J. Phys. D: Appl. Phys. 49, 045303 (2016)

[27] R. Alvarez, J. M. Garcia-Martin, M. Macias-Montero, L Gonzalez-Garcia, J. C. Gonzalez, V. Rico, J. Perlich, J. Cotrino, A. R. González-Elipe and A. Palmero, Nanotechnology 24, 045604 (2013)

[28] M. Pelliccione and T.-M Lu Evolution of Thin Film Morphology: Modeling and Simulations (Springer Series: Materials Science, vol 108) (Berlin: Springer) 2008

[29] R. Alvarez, P. Romero-Gomez, J. Gil-Rostra, J. Cotrino, F. Yubero, A. Palmero, A.R. Gonzalez-Elipe, J. Appl. Phys. 108(6), 064316 (2010)

[30] K. Nakata, A. Fujishima, J. Photochem. Photobiol. C 13(3), 169 (2012)

[31] S.J. Baim C.M. Ki, J.F. Zang, X.Q. Cui, Y, Qiao, J. Guo, Adv. Funct. Mater. 18(4), 591 (2008)

[32] T. Kuschel, A. von Keudell, J. Appl. Phys. 107(10), 103302 (2010)

[33] J. Musil, P. Baroch, J. Vlcek, K.H.Nam, J.G. Han, Thi Solid Films 475, 208 (2005)

[34] A. Siad, A. Besnard, C. Nouveau, P. Jacquet, Vacuum 131, 305 (2016)

[35] K. van Aeken, SIMTRA available at www.draft.ugent.be

[36] K. van Aeken, S. Mahieu, D. Depla, J. Phys. D: Appl. Phys 41, 20530 (2008)

[37] The Software SRIM is available at http://www.srim.org

[38] The Software OPTIFIT is available at: http://nanoscops.icmse.csic.es

[39] R. Alvarez, P. Romero-Gomez, J. Gil-Rostra, J. Cotrino, F. Yubero, A.R. Gonzalez-Elipe, A. Palmero, Phys, Status Solidi A 210(4) 796 (2013)

[40] M. Khardani, M. Bouaïcha, B. Bessaïs, Phys. Stat. Solid. 4(6), 1986 (2007)

Table I

Conditions	Pressure (*Pa*)	Incident Polar Angle (º)	Deposition Time (h)	Tilt Angle (º)	*L* *(cm)*	L_C *(cm)*
#1	0.5	80	3.5	95	7	--
#2	0.5	80	6.0	95	7	2
#3	0.2	80	3.5	95	7	--
#4	0.2	80	6.0	95	7	2
#5	0.8	80	3.5	95	7	--
#6	0.8	80	6.0	95	7	2
#7	0.8	0	6.0	0	10	5

Table I.- List of deposition conditions. In this table, *L* refers to the distance between the target and the substrate, whereas L_c to the length of the base of the collimator.

Figure Caption

Figure 1.- a) Picture of the collimator employed in conditions #1-#6 in Table I. b) Scheme of the reactor configuration under conditions #1-#6 in Table I. c) Scheme of the reactor configuration under condition #7.

Figure 2.- Incident polar angle distribution of deposition species and the ballistic, thermalized and partially-thermalized components. The theoretical shape of species that follow an isotropic momentum distribution is also depicted along with the incident polar angle distribution of deposition species when using the collimator. a) conditions #1 and #2, b) conditions #3 and #4, and c) conditions #5 and #6. Areas of the curves are proportional to the number of deposited particles in each case.

Figure 3.- Cross-sectional SEM images of thin films grown in a) conditions #1, b) conditions #2, c) conditions #3, d) conditions #4, e) conditions #5, and f) conditions #6.

Figure 4.- a) Film thickness as a function of the distance from the vertex of the collimator in conditions #7 in Table I, along with cross-sectional SEM images at those positions. b) Scheme of the different angular restrictions imposed by the collimator at different substrate positions. c) Incident polar angle distribution function of deposition species in case #7 as a function of the distance from the vertex of the collimator. Areas of the curves are proportional to the number of deposited particles in each case.

Figure 1.

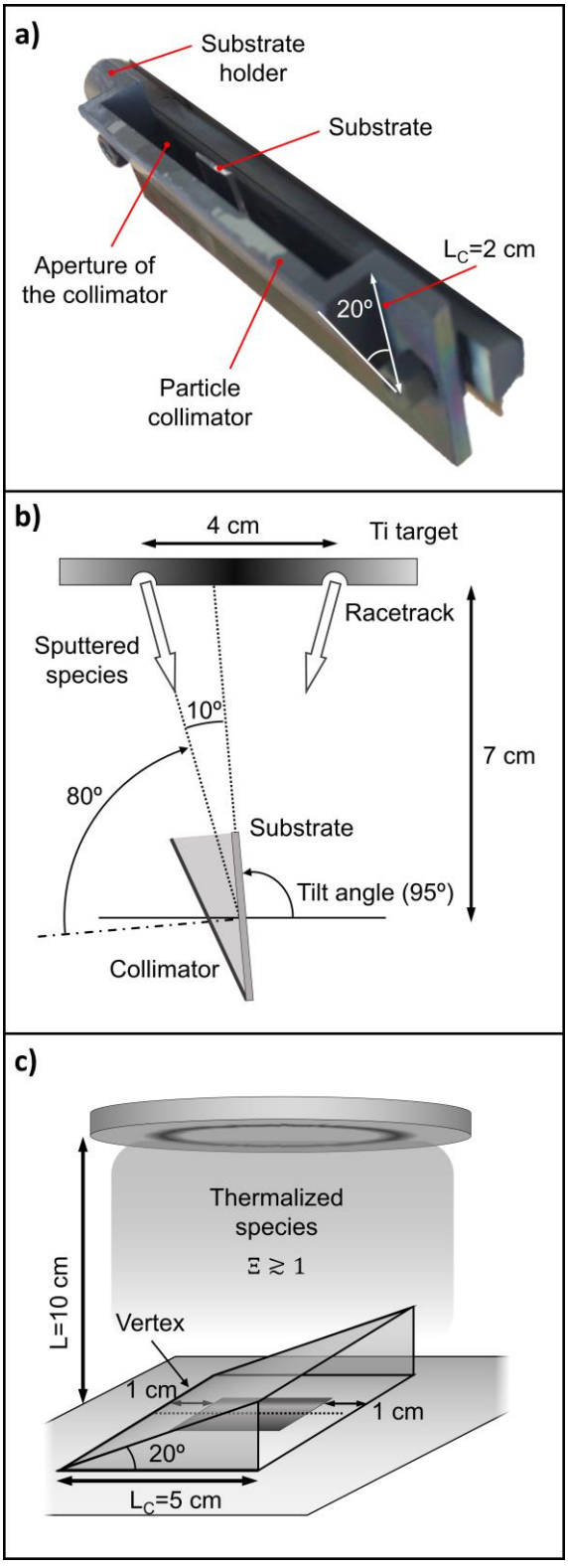
a)
Substrate holder
Substrate
Aperture of the collimator
L_C=2 cm
20º
Particle collimator
b)
4 cm
Ti target
Racetrack
Sputtered species
10º
7 cm
80º
Substrate
Tilt angle (95º)
Collimator
c)
Thermalized species
Ξ ≳ 1
L=10 cm
Vertex
1 cm
1 cm
20º
L_C=5 cm

Figure 2

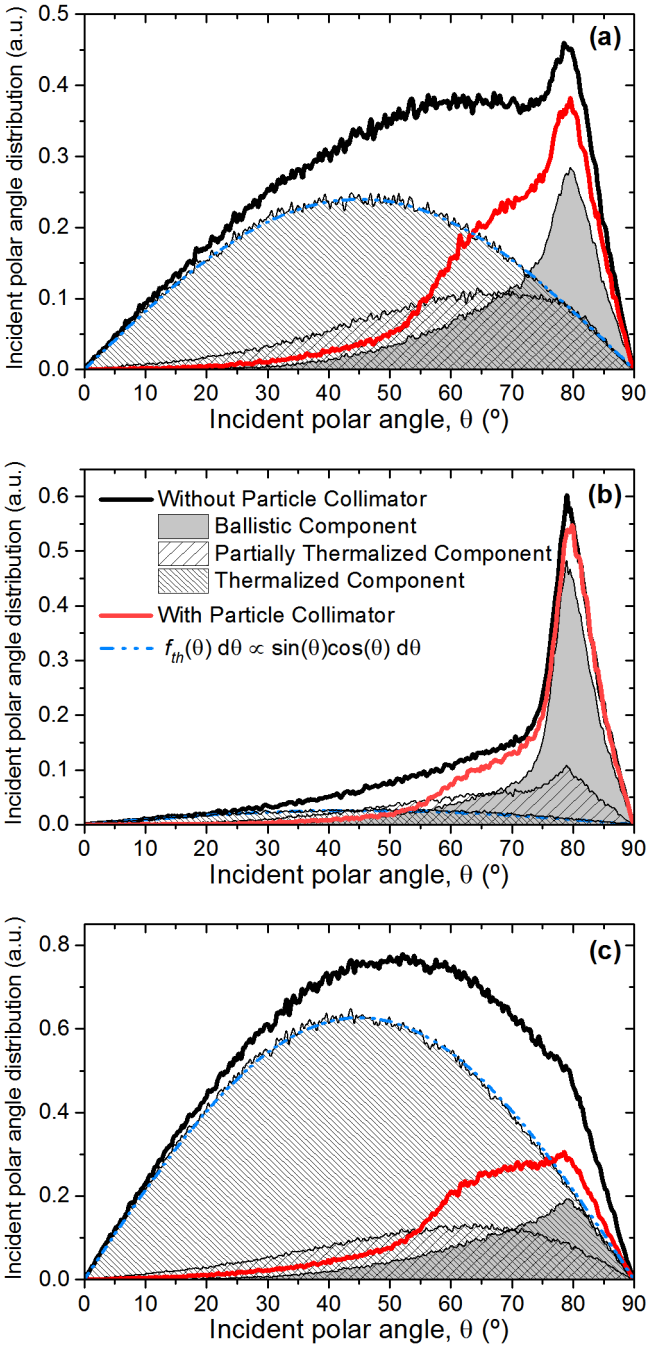
(a)
Incident polar angle distribution (a.u.)
Incident polar angle, θ (°)
(b)
Without Particle Collimator
Ballistic Component
Partially Thermalized Component
Thermalized Component
With Particle Collimator
$f_{th}(\theta)\, d\theta \propto \sin(\theta)\cos(\theta)\, d\theta$
Incident polar angle distribution (a.u.)
Incident polar angle, θ (°)
(c)
Incident polar angle distribution (a.u.)
Incident polar angle, θ (°)

Figure 3

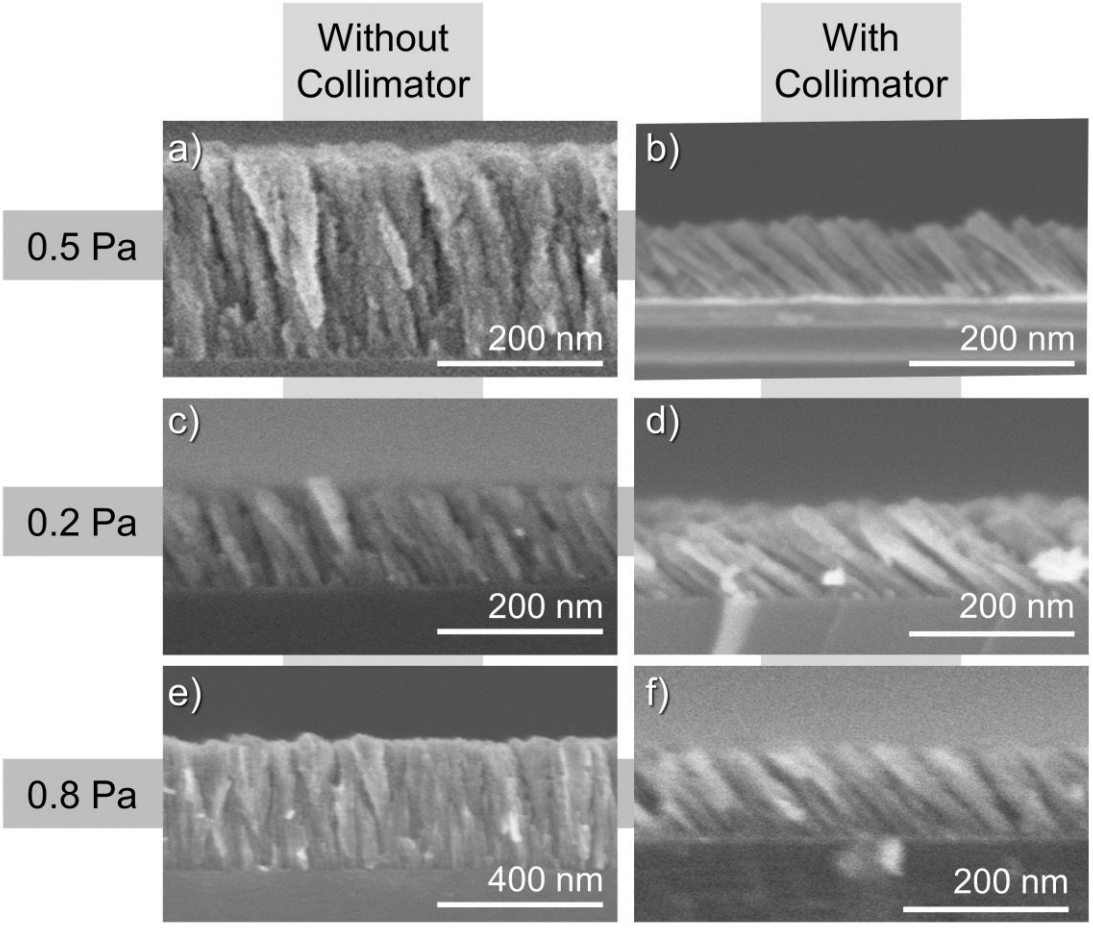
Without Collimator
With Collimator
0.5 Pa
0.2 Pa
0.8 Pa
a)
b)
c)
d)
e)
f)
200 nm
200 nm
200 nm
200 nm
400 nm
200 nm

Figure 4

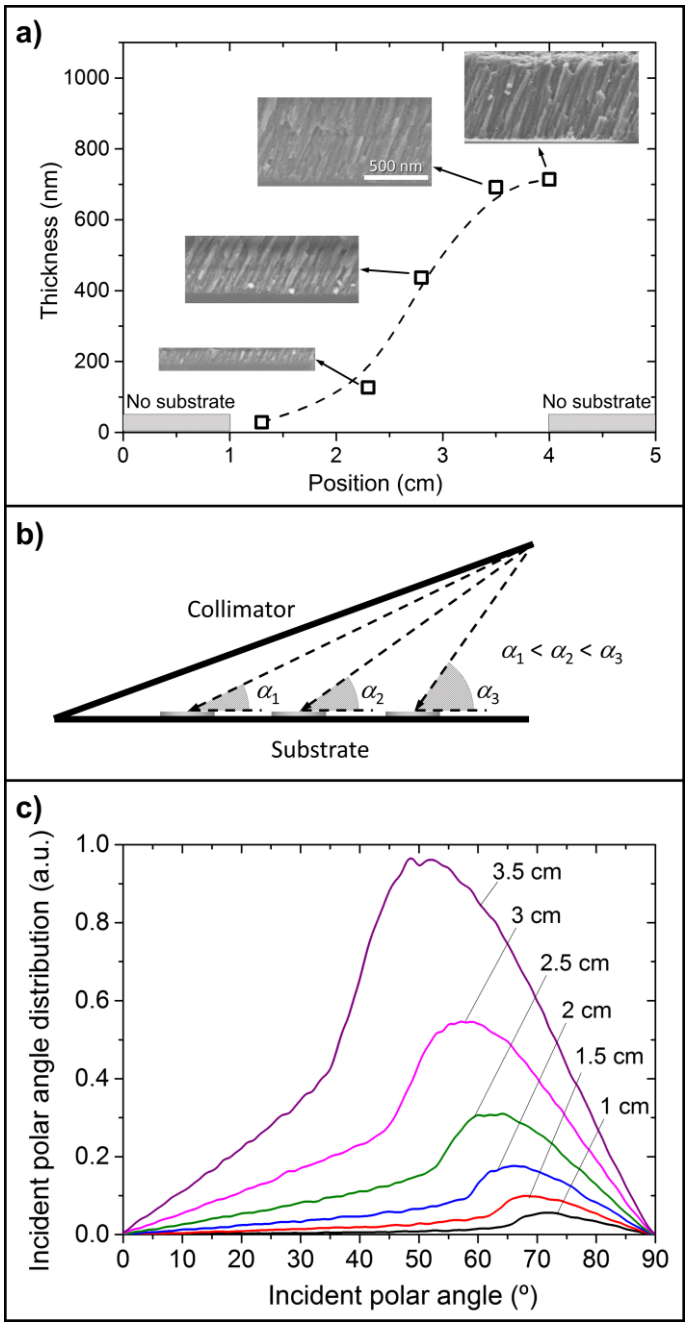
a)
Thickness (nm)
Position (cm)
500 nm
No substrate
No substrate
b)
Collimator
$\alpha_1 < \alpha_2 < \alpha_3$
α_1
α_2
α_3
Substrate
c)
Incident polar angle distribution (a.u.)
Incident polar angle (°)
3.5 cm
3 cm
2.5 cm
2 cm
1.5 cm
1 cm